AIAA Propulsion and Energy Forum
19-22 August 2019, Indianapolis, IN
AIAA Propulsion and Energy 2019 Forum

10.2514/6.2019-4467

Check for updates

A High Efficiency Low Noise VTOL/ESTOL Concept Using CoFLow Jet Airfoil

Gecheng Zha [*] Yan Ren [†] Jiaye Gan [‡] Daniel Espinal [§]
Dept. of Mechanical and Aerospace Engineering
University of Miami
Coral Gables, Florida 33124
E-mail: gzha@miami.edu

Downloaded by Gecheng Zha on September 27, 2019 | http://arc.aiaa.org | DOI: 10.2514/6.2019-4467

Abstract

This paper proposes a novel air vehicle concept that has the VTOL and ESTOL capability naturally combined together using CoFlow Jet(CFJ) active flow control airfoil. The CFJ-VTOL system is an integrated system with propellers mounted above the CFJ wing suction surface. Different from the conventional VTOL systems that rely solely on the propellers completely facing upward to generate the vertical lift, the propellers of the CFJ-VTOL system faces forward and upward and only generate a part of the total lift. An important function of the propellers is to pull flow to the CFJ airfoil at static condition. The CFJ airfoil then generates very high lift coefficient at extraordinarily high angle of attack(e.g. $> 70°$) with a much lower power consumption rate than the propellers. In other words, the CFJ-VTOL makes use of the CFJ wing to generate substantial or even the majority of the lift at vertical takeoff and landing, whereas the wings of conventional VTOL aircraft generate no lift at takeoff and landing even though they produce all the lift at cruise. Such an integrated CFJ-VTOL system has the potential to reduce the power loading by 20% or more at the VTOL phase. For the same lift coefficient, the disk loading is significantly reduced with a benefit to decrease the noise. Furthermore, the upper wing mounted propeller is shield by the wing to mitigate downward radiating noise of the propeller. The maximum injection jet Mach number is 0.3 - 0.4, is at fairly low level for jet noise. The CFJ-VTOL system hence is also potentially much quieter than the conventional VTOL. The resultant force of the propeller-CFJ airfoil system at the static condition is controlled by the airfoil orientation angle. By rotating the same propeller-CFJ airfoil system forward, the system can generate both very high lift and thrust for ESTOL, which further reduces the power consumption and noise level compared with the VTOL system. The same system can be potentially used either for VTOL or ESTOL depending on the situation with significantly reduced takeoff/landing power and noise. This paper presents the numerical results evidencing the advantages by 2D CFJ-VTOL airfoil and 3D wing simulations.

Nomenclature

CFJ Co-flow jet

[*] Professor, AIAA Associate Fellow, President of CoFLow Jet, LLC
[†] Postdoc Researcher, Ph.D., AIAA member
[‡] Ph.D. Candidates
[§] Ph.D. Candidates

Copyright © 2019 by all the authors of this paper . Published by the American Institute of Aeronautics and Astronautics, Inc., with permission.

AoA	Angle of attack
LE	Leading Edge
TE	Trailing Edge
β_{max}	Maximum Injection Duct Inlet Swirl Angle
S	Planform area
s	Wing Span length
c	Profile chord
U	Flow velocity
q	Dynamic pressure $0.5\,\rho\,U^2$
p	Static pressure
ρ	Air density
$\dot{m}$	Mass flow
M	Mach number
ω	Pitching Moment
P	Pumping power
ΔP	Pressure percentage increase across the propeller actuator disk
PL	Power loading, power/lift
DL	Disk loading, thrust of the actuator disk/actuator disk area
PL_c	Power loading coefficient
DL_c	Disk loading coefficient
F_c	Resultant force coefficient $F/(q_\infty S)$
AR	Wing aspect ratio
PR	Total pressure ratio of the CFJ injection to suction
∞	Free stream conditions
$_j$	Jet conditions
C_L	Lift coefficient $L/(q_\infty\,S)$
C_D	Drag coefficient $D/(q_\infty\,S)$
C_m	Pitching moment coefficient $M_{c/4}/(q_\infty\,Sc)$
C_μ	Jet momentum coef. $\dot{m}_j\,U_j/(q_\infty\,S)$
P_c	CFJ power coefficient $P/(q_\infty\,S\,V_\infty)$
P_P	Propeller actuator power coefficient $\frac{2}{\rho V_\infty^3 S}\sqrt{\frac{F^3}{2\rho A}}$
$(C_L^2/C_D)_c$	CFJ airfoil corrected productivity efficiency $C_L^2/(C_D+P_c)$

Downloaded by Gecheng Zha on September 27, 2019 | http://arc.aiaa.org | DOI: 10.2514/6.2019-4467

1 Introduction

Recent global efforts in decreasing emission pollution and reducing city traffic congestion has fostered a strong growth of technology development for electric personal air vehicle with vertical takeoff/landing(VTOL) capability[1]. VTOL has an appealing advantage for urban transportation due to its independence of runways. However, so far there are no mature urban VTOL air vehicle products in the market yet.

For urban VTOL personal air vehicle, Distributed Electric Propulsion aircraft(DEPA) powered by batteries are considered as a superior platform to conventional helicopter systems. DEPA has great potential to provide several crucial advantages, including lower noise, faster cruise speed, higher cruise efficiency, higher safety due to high propulsion system redundancy, higher stability, easier operation, higher passenger comfort, lower cost for manufacturing and operation, and being fully autonomous.

Noise is a very challenging issue that urban VTOL aircraft need to overcome to receive wide public acceptance[1]. It should be hardly audible when cruising in the air and has a noise level comparable to community background noise at takeoff and landing. Quantitatively, a reasonable noise goal for urban VTOL vehicles is 67 dB(A) at ground level from a VTOL at 250 ft altitude as indicated by Uber[1].

As a general principle, the motor and propeller system weight is sized by the maximum power required at takeoff/landing, which is not needed at cruise and will penalize the cruise and mission efficiency performance. The higher the cruise speed, the higher the penalty due to VTOL requirement, and the higher the noise at VTOL phase. Hence a high efficiency and quiet VTOL system should have a low VTOL power requirement to minimize the energy consumption and weight.

Almost all the current Distributed Electric Propulsion(DEP) systems for VTOL aircraft utilize multiple propellers generating vertical lift by either articulating the propellers or rotating the wings with propellers to vertical lifting direction. Such systems can be seen in the VTOL aircraft of Zee Aero, Joby Aviation, A^3/AirBus Vahana18, Lilium, etc. The advantage of multiple propellers is that each of the propellers will have smaller size than the single rotor of helicopters and hence has lower tip rotating speed and low relative flow speed, which may significantly reduce the noise level. However, such direct vertical lifting(DVL) requires very high power and energy consumption. In addition, the required disk loading and unshielded propellers still make VTOL vehicles very noisy. For VTOL aircraft with DVL, the wings that generate all the lift at cruise have little contribution to the lift at takeoff and landing.

Compared with the DVL, the conventional takeoff/landing(CTOL) air vehicles using runways is much more energy efficient and quiet with electric motors. The reason is that the lifting process of CTOL relies on the lift generated by the wing with the dynamic pressure from the free stream, the wing lift coefficient, and the wing surface area. The power and energy consumption is much smaller than VTOL aircraft. In addition, the noise level is also substantially lower due to low propeller disk loading.

It is appealing if VTOL aircraft can combine the advantages of the direct vertical lifting and CTOL to enhance the overall lift from the wings. Such technology has great potential to dramatically reduce the noise level of VTOL aircraft and increase the efficiency of the system. Furthermore, it is desirable if a VTOL air vehicle can also perform ESTOL(extremely short takeoff/landing) when there is a short run way available. The ESTOL is a type of CTOL and hence requires significantly lower power consumption than VTOL. The recent co-flow jet (CFJ) airfoil technology developed by Zha and his team is promising to provide a high efficiency low noise VTOL platform, which at the same time possesses the ESTOL capability with further reduced energy consumption and noise level. [2, 3, 4, 5, 6, 7, 8, 9, 10, 11, 12, 13, 14].

Downloaded by Gecheng Zha on September 27, 2019 | http://arc.aiaa.org | DOI: 10.2514/6.2019-4467

2 The Co-Flow Jet Airfoil

The CFJ airfoil has an injection slot near the leading edge(LE) and a suction slot near the trailing edge(TE) on the airfoil suction surface as sketched in Fig. 1. A small amount of mass flow is withdrawn into the airfoil near the TE, pressurized and energized by a micro-compressor system inside the airfoil, and then injected near the LE in the direction tangent to the main flow. The whole process does not add any mass flow to the system and hence is a zero-net mass-flux flow control.

The CFJ airfoil flow control mechanism achieves a radical lift augmentation, drag reduction and stall margin increase at a very low energy expenditure. It can not only achieve ultra-high maximum lift coefficient, but also significantly enhance cruise productivity efficiency and cruise wing loading from subsonic to transonic conditions[11, 12, 9, 13, 14, 15].

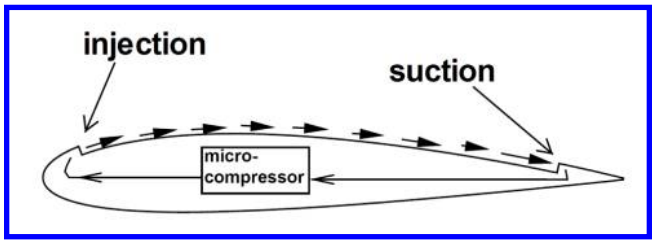

Figure 1: Baseline airfoil and CFJ Airfoil.

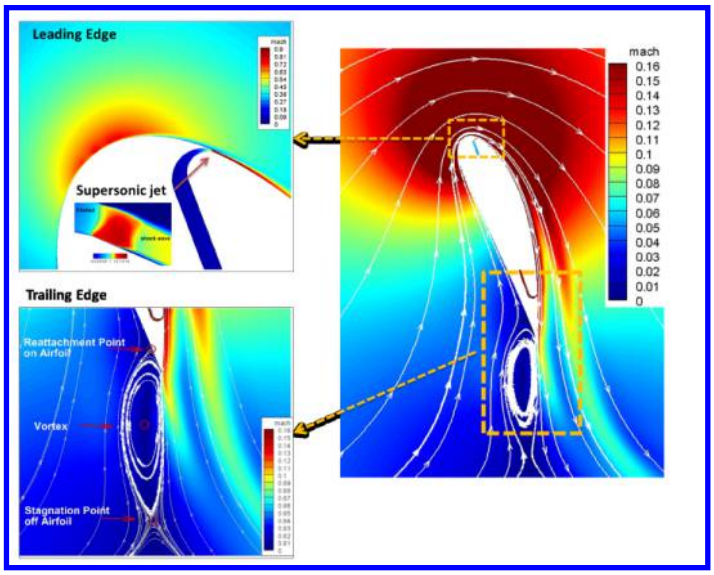

Figure 2: Mach number contours and streamlines at $C_\mu = 0.35$ and AoA =70° for the CFJ6421-SST016-SUC053-INJ009 airfoil.

Yang and Zha [14] discovered in 2017 that a CFJ airfoil can achieve Super-Lift Coefficient(SLC), which is a lift coefficient that exceeds the theoretical limit of potential flow developed by Smith[16] and is defined below:

$$C_{Lmax} = 2\pi(1 + \frac{t}{c}) \tag{1}$$

When a SLC occurs, the circulation is so high that the stagnation point is detached from the airfoil body as shown in Fig. 2, which has a C_{Lmax} of 10.6, far greater than the theoretical limit of 7.6. The freestream condition has a Mach number of 0.063 and Reynolds number of 3 million. The flow remains attached at AoA of 70° and the wake is filled with reversed velocity deficit, similar to the owl effect that generates very low wake turbulent noise. The CFJ airfoil pressure coefficient at the leading edge suction peak is nearly 10 times higher than the maximum value of the baseline airfoil at AoA of 18° before it stalls [14]. In other words, the CFJ airfoil at SLC condition can keep flow attached despite an adverse pressure gradient nearly one order of magnitude higher than the conventional airfoil. The simulation of Yang and Zha [14] also reveals a complex phenomenon with 4 layers of counter-rotating vortex layers emanating from leading edge and trailing to the wake of the airfoil. The detailed analysis can be seen in [14, 17].

The Super-Lift Coefficient of CFJ airfoil is recently proved by wind tunnel experiment. Fig. 3 is the photo of the CFJ-NACA6421 airfoil recently tested in wind tunnel[15]. The airfoil has a dimension of 0.72m (chord) × 2.1m (span) with 5 micro-compressors embedded along the span as shown in Fig. 4. A CFJ airfoil is a completely self-contained system with no need to use any other air flow source for the jet.

The micro-compressor actuators have an outer diameter of 84mm and length of 124mm designed with mixed centrifugal and axial compressor flow path. The mass flow rate can be varied from about 20g/s to 80g/s with the pressure ratio varying from 1.05 to 1.4. The power of the compressor is varied from 200w to 2kw with the RPM varying from 70k to 145k. The micro-compressor is customer designed based on our CFD design and simulation of the CFJ airfoil matching the wind tunnel conditions.

Downloaded by Gecheng Zha on September 27, 2019 | http://arc.aiaa.org | DOI: 10.2514/6.2019-4467

Figure 3: Photo of the CFJ-NACA-6421 airfoil tested.

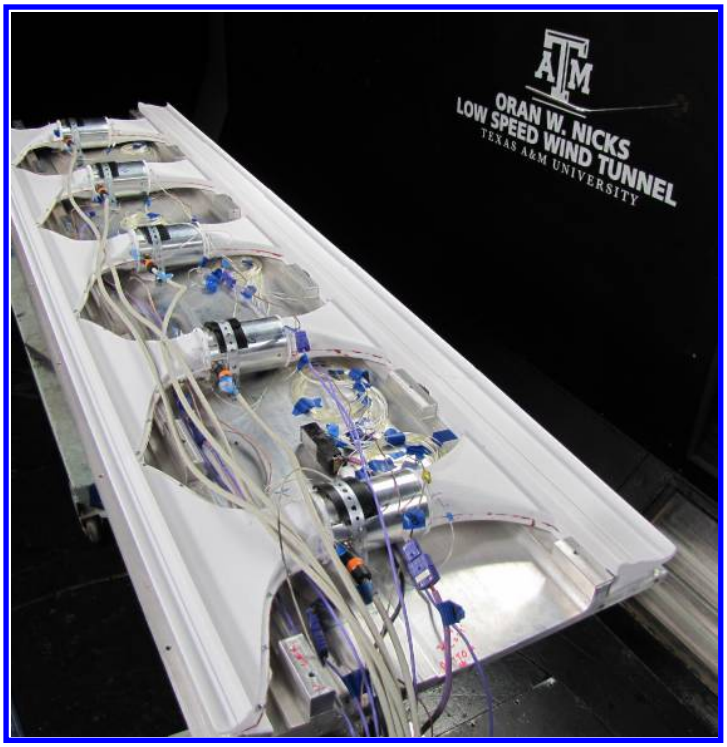

Figure 4: Photo of the tested CFJ-NACA-6421 airfoil with 5 micro-compressors embedded.

Fig. 5, 6 and 7 are the coefficient of lift, drag and pitching moment of the CFJ airfoil achieving super-lift coefficient compared with the baseline NACA6421 airfoil with no CFJ.

The maximum thrust coefficient is very high up to C_D= -1.0 at low AoA as shown in Fig. 6. The CFJ thrust in the experiment is achieved with a wide range AoA up to 40° before the airfoil is stalled. The baseline airfoil drag is positive for all the AoA tested as usual. The CFJ airfoil appears to be the only man made airfoil that can generate ultra-high lift and thrust simultaneously without flapping as bird wings. The CFJ wing is naturally a distributed propulsion system, which tightly and efficiently integrates the propulsion with the wing.

As shown in Fig. 7, the nose down pitching moment coefficient is substantially higher than that of the baseline airfoil at low AoA due to the increased lift, but is rapidly decreased when the AoA is increased with the shortened moment arm and increased front loading at leading edge due to the super-suction effect.

The CFJ airfoil has very low energy expenditure, because the jet is injected at the leading edge peak suction location, where the main flow pressure is near the lowest and it hence requires a low power to eject the flow, and it is sucked at the trailing edge, where the main flow pressure is near the highest and it hence requires a low power for the flow to be sucked into the airfoil. The low energy expenditure is the key factor enabling the CFJ airfoil not just to achieve ultra-high lift coefficient at high AoA, but also to possess a unique capability to improve aerodynamic efficiency at cruise when the flow is benign at low AoA from subsonic to transonic [9, 11, 13].

Downloaded by Gecheng Zha on September 27, 2019 | http://arc.aiaa.org | DOI: 10.2514/6.2019-4467

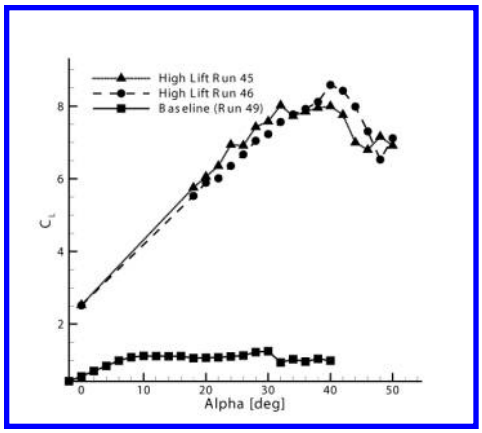

Figure 5: Lift coefficient of the Super-Lift CFJ airfoil and baseline airfoil vs AoA.

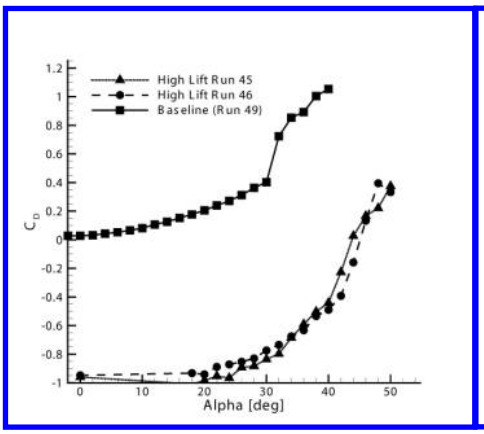

Figure 6: Drag coefficient vs AoA.

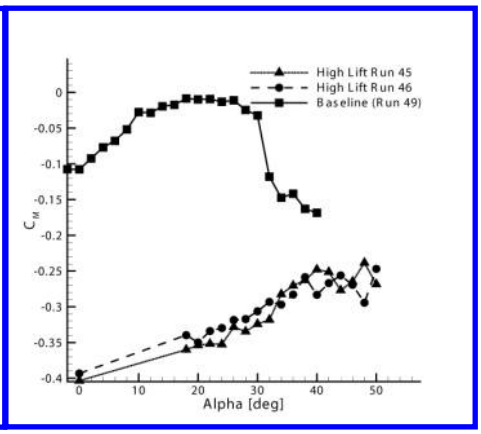

Figure 7: Pitching Moment coefficient vs AoA.

3 A Novel VTOL Concept Using CoFlow Jet Airfoil(CFJ-VTOL)

The new CFJ-VTOL concept is to utilize the superior CFJ airfoil with propeller for VTOL aircraft to generate substantial lift from the CFJ airfoil instead of generating all the lift from the propeller. The CFJ airfoil as demonstrated in the previous section can sustain very high angle of attack and generate very high lift coefficient with no stall. However, at static condition, the CFJ airfoil itself will not generate high lift unless there is freestream flowing toward the airfoil.

The CFJ-VTOL concept is depicted in Fig. 8, which has a propeller mounted on the upper surface of a CFJ airfoil. The propeller does not completely face upward as conventional VTOL aircraft that rely on the propellers to generate all the lift. The propeller of CFJ-VTOL faces forward and upward as shown in Fig. 8. It generates a partial lift for the VTOL system and induces freestream to the CFJ airfoil at the static condition. Enhanced by the freestream, the CFJ airfoil at a very high angle of attack(e.g. $> 70°$) will generate a ultra-high lift coefficient at a much lower power consumption than the propellers. The CFJ airfoil will produce substantial portion or even the majority of the total lift. To achieve a certain lift, the propeller disk loading will be largely lower than typical VTOL aircraft since it does not play the role as the sole generator of vertical lift. The low propeller disk loading will significantly reduce the VTOL noise level. In addition, the propeller noise radiating to ground will be substantially shielded by the wing surface.

Downloaded by Gecheng Zha on September 27, 2019 | http://arc.aiaa.org | DOI: 10.2514/6.2019-4467

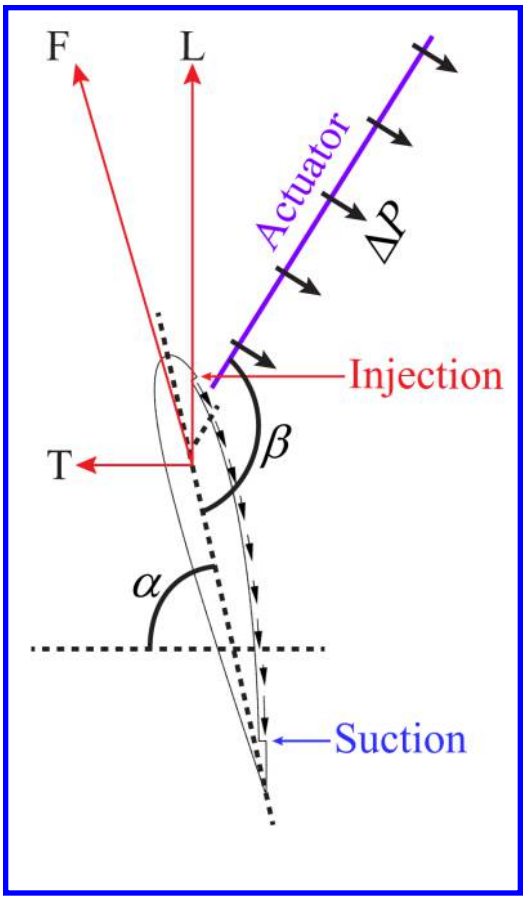

Figure 8: Schematic plot of a typical CFJ airfoil in VTOL/ESTOL condition.

3.1 VTOL and ESTOL in One System

The same VTOL system can be used for an extremely short takeoff/landing(ESTOL) aircraft. The resultant force coefficient F_C of the propeller-CFJ airfoil system illustrated in Fig. 8 has the following relation:

$$F_C = f(\alpha, \beta, V_\infty, P_C, P_P) \tag{2}$$

where α is the angle between the CFJ airfoil chord and the horizontal direction, β the angle between the airfoil chord and the propeller disk, P_C the power coefficient of CFJ defined in Eq. 10, P_P the power coefficient of the propeller actuator defined in Eq. 11. In general, increasing $\alpha, \beta,\ P_C,\ P_P$ will increase F_C provided the flow is remained attached. At the static condition with $V_\infty = 0$, if $\beta,\ P_C,\ P_P$ are fixed, the magnitude of F_C is constant and the direction is only determined by α.

At the static condition with an α that generates the resultant force pointing vertically upward, the system is for VTOL. When the α is decreased from the VTOL angle, the resultant force will point to forward and upward for ESTOL with a thrust. In other words, the same propeller-CFJ airfoil system can be used for both VTOL and ESTOL by controlling the CFJ wing chord angle. The ESTOL will substantially decrease the power consumption than the VTOL. This provides versatile features for an air vehicle. When there is no space as for a run way, the vehicle can choose VTOL mode. When there is a small space used as a runway, the air vehicle can choose ESTOL mode to save energy.

Downloaded by Gecheng Zha on September 27, 2019 | http://arc.aiaa.org | DOI: 10.2514/6.2019-4467

4 CFJ Parameters

The following are the parameters used to define the CFJ airfoil performance.

4.1 Lift and Drag Calculation

The momentum and pressure at the injection and suction slots produce a reactionary force, which is automatically measured by the force balance in wind tunnel testing. However, for CFD simulation, the full reactionary force needs to be included. Using control volume analysis, the reactionary force can be calculated using the flow parameters at the injection and suction slot opening surfaces. Zha et al. [2] give the following formulations to calculate the lift and drag due to the jet reactionary force for a CFJ airfoil. By considering the effects of injection and suction jets on the CFJ airfoil, the expressions for these reactionary forces are given as :

$$F_{x_{cfj}} = (\dot{m}_j V_{j1} + p_{j1} A_{j1}) * cos(\theta_1 - \alpha) - (\dot{m}_j V_{j2} + p_{j2} A_{j2}) * cos(\theta_2 + \alpha) \tag{3}$$

$$F_{y_{cfj}} = (\dot{m}_{j1} V_{j1} + p_{j1} A_{j1}) * sin(\theta_1 - \alpha) + (\dot{m}_{j2} V_{j2} + p_{j2} A_{j2}) * sin(\theta_2 + \alpha) \tag{4}$$

where the subscripts 1 and 2 stand for the injection and suction respectively, and θ_1 and θ_2 are the angles between the injection and suction slot's surface and a line normal to the airfoil chord. α is the angle of attack.

The total lift and drag on the airfoil can then be expressed as:

$$D = R'_x - F_{x_{cfj}} \tag{5}$$

$$L = R'_y - F_{y_{cfj}} \tag{6}$$

where R'_x and R'_y are the surface integral of pressure and shear stress in x (drag) and y (lift) direction excluding the internal ducts of injection and suction. For CFJ wing simulations, the total lift and drag are calculated by integrating Eqs.(5) and (6) in the spanwise direction.

4.2 Jet Momentum Coefficient

The jet momentum coefficient C_μ is a parameter used to quantify the jet intensity. It is defined as:

$$C_\mu = \frac{\dot{m} V_j}{\frac{1}{2} \rho_\infty {V_\infty}^2 S} \tag{7}$$

where $\dot{m}$ is the injection mass flow, V_j is the mass-averaged injection velocity, ρ_∞ and V_∞ denote the free stream density and velocity, and S is the planform area.

Downloaded by Gecheng Zha on September 27, 2019 | http://arc.aiaa.org | DOI: 10.2514/6.2019-4467

4.3 Power Coefficient

CFJ is implemented by mounting a pumping system inside the wing that withdraws air from the suction slot and blows it into the injection slot. The power consumption is determined by the jet mass flow and total enthalpy change as the following:

$$P_{CFJ} = \dot{m}(H_{t1} - H_{t2}) \tag{8}$$

where H_{t1} and H_{t2} are the mass-averaged total enthalpy in the injection cavity and suction cavity respectively, P is the Power required by the pump and $\dot{m}$ the jet mass flow rate. Introducing P_{t1} and P_{t2} the mass-averaged total pressure in the injection and suction cavity respectively, the pump efficiency η, and the total pressure ratio of the pump $\Gamma = \frac{P_{t1}}{P_{t2}}$, the power consumption is expressed as:

$$P_{CFJ} = \frac{\dot{m} C_p T_{t2}}{\eta}(\Gamma^{\frac{\gamma-1}{\gamma}} - 1) \tag{9}$$

where γ is the specific heat ratio equal to 1.4 for air. The power coefficient for CFJ is expressed as:

$$P_c = \frac{P_{CFJ}}{\frac{1}{2}\rho_\infty V_\infty^3 S} \tag{10}$$

The power coefficient for the propeller actuator is:

$$P_P = \frac{2}{\rho V_\infty^3 S}\sqrt{\frac{F^3}{2\rho A}} \tag{11}$$

where A is the actuator disk area; F is the total force produced by the propeller actuator normal to the propeller disk.

In order to compare the efficiency of a CFJ airfoil with that of a conventional airfoil, a corrected aerodynamic efficiency $(L/D)_c$ is introduced, which takes into consideration the power needed for the CFJ[9] as the following:

$$(\frac{C_L}{C_D})_c = \frac{L}{D + \frac{P}{V_\infty}} = \frac{C_L}{C_D + P_C} \tag{12}$$

where V_∞ is the free stream velocity, P is the CFJ pumping power, L and D are the lift and drag generated by the CFJ airfoil, and C_L, C_D and P_C are the coefficient of lift, drag and CFJ pumping power. The $(L/D)_c$ incorporates the CFJ power consumed into the drag of the airfoil.

For a full electric battery powered airplane, the aircraft weight will not change during flight. The productivity parameter measuring the an airplane's capability to transport its gross weight for a maximum range is defined as:

$$C_{RW} = \frac{RW}{\frac{1}{2c}\rho V_\infty^2 S E_c/g} = \eta \frac{C_L^2}{C_D}\frac{W_b}{W_0} \tag{13}$$

where R is the range, W is the weight, E_c is the battery specific energy density (Wh/kg), W_b is the total battery weight, η is the propeller efficiency.

Downloaded by Gecheng Zha on September 27, 2019 | http://arc.aiaa.org | DOI: 10.2514/6.2019-4467

For the same battery energy density, to compare the aircraft with the same ratio of initial weight to final weight, the only factor affecting their productivity parameter is C_L^2/C_D. The parameter C_L^2/C_D is hence named productivity efficiency[14]. The productivity efficiency is considered as a more comprehensive parameter than the conventional aerodynamic efficiency C_L/C_D to measure the merit of an airplane aerodynamic design for cruise performance. The former includes not only the information of C_L/C_D, but also the information of the aircraft weight represented by C_L.

For CFJ airfoil, the productivity efficiency should also include the CFJ power consumption and is defined as below:

$$\frac{C_L^2}{C_{Dc}} = \frac{C_L^2}{C_D + P_C} \tag{14}$$

For CFJ airfoil, the minimum CFJ pumping power occurs at a fairly high AoA [8, 9]. With the augmentation of CFJ, the subsonic cruise lift coefficient of a CFJ airfoil is typically 2 to 3 times higher than the conventional airfoil with about the same $(C_L/C_D)_c$ [12]. Such a high lift coefficient is unattainable for conventional airfoil since they would be either stalled or near stalled with very high drag. Hence for CFJ aircraft design, the productivity efficiency $C_L^2/C_{Dc} = C_L(C_L/C_D)_c$ is more informative to be used to reflect the aerodynamic performance.

4.4 Disk Loading and Power Loading at Hovering Condition

Disk loading and power loading are used to describe rotorcraft VTOL performance. The disk loading (DL) is defined as $DL = L/A$, where L is the lift normal to the propeller disk and A is the propeller disk area. It is closely related to the noise produced by the actuator disk. The power loading (PL) for a propeller disk at static hovering condition is defined as $PL = P/L$, where P is the propeller power at the generated lift L. The power loading indicates the power required per unit lift for rotorcraft. The disk loading and power loading coefficients are defined as follows:

$$DL_c = \frac{DL}{\frac{1}{2}\rho V_\infty^2} = \frac{C_L}{A_c} \tag{15}$$

where $C_L = L/(0.5\rho V^2 S)$, $A_c = A/S$, A is the disk area and S is the wing planform area.

$$PL_c = \frac{PL}{V_\infty} = \frac{P_{\square}}{C_L} \tag{16}$$

The actuator DL and PL has the following relations in hovering condition:

$$PL = \sqrt{DL\frac{1}{2\rho}} \tag{17}$$

$$PL_c = \frac{\sqrt{DL_c}}{2} \tag{18}$$

For the CFJ-VTOL system at hovering condition, the propeller disk may not be fully facing upward as shown in Fig. 8. The disk loading showing the disk load should be defined as:

Downloaded by Gecheng Zha on September 27, 2019 | http://arc.aiaa.org | DOI: 10.2514/6.2019-4467

$$DL = \frac{F}{A} \tag{19}$$

where, the F is the resultant force normal to the propeller disk. The power loading to describe the power required per unit lift is still defined as:

$$PL = P/L \tag{20}$$

For a CFJ-VTOL system, the lift will be generated by both the propeller and the wing. Thus the power loading can be used for the whole system or for each component such as the propeller or the wing.

For the system,

$$PL_{CFJ-VTOL} = \frac{P_{CFJ} + P_{actuator}}{L_{CFJ} + L_{actuator}} \tag{21}$$

For the component,

$$PL_{CFJ} = \frac{P_{CFJ}}{L_{CFJ}} \tag{22}$$

$$PL_{actuator} = \frac{P_{actuator}}{L_{actuator}} \tag{23}$$

Please note

$$PL_{CFJ-VTOL} \neq PL_{CFJ} + PL_{actuator} \tag{24}$$

4.5 CFD Simulation Setup

The in house FASIP (Flow-Acoustics-Structure Interaction Package) CFD code is used to conduct the numerical simulation. The 2D/3D Improved Delayed Detached-Eddy Simulation (IDDES) turbulence model is used. A 3rd order WENO scheme for the inviscid flux [18, 19, 20, 21, 22, 23] and a 2nd order central differencing for the viscous terms [18, 22] are employed to discretize the Navier-Stokes equations. The low diffusion E-CUSP scheme used as the approximate Riemann solver suggested by Zha et al [19] is utilized with the WENO scheme to evaluate the inviscid fluxes. Implicit time marching method using Gauss-Seidel line relaxation is used to achieve a fast convergence rate [24]. Parallel computing is implemented to save wall clock simulation time [25].

Downloaded by Gecheng Zha on September 27, 2019 | http://arc.aiaa.org | DOI: 10.2514/6.2019-4467

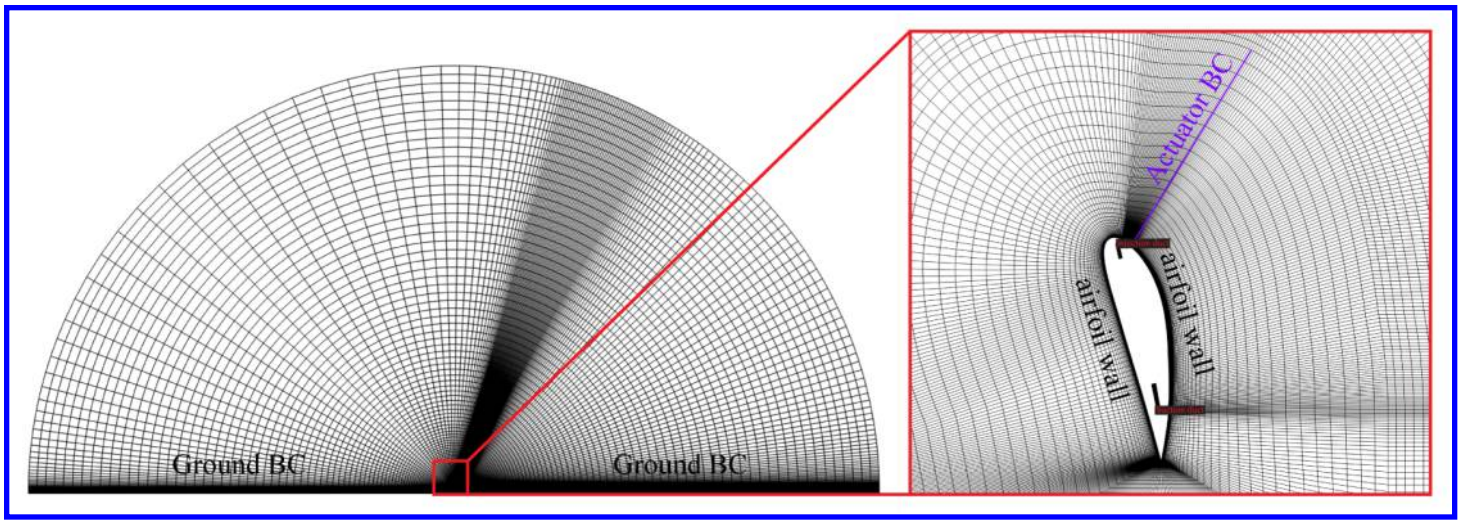

Figure 9: Computational mesh used in the current work.

Downloaded by Gecheng Zha on September 27, 2019 | http://arc.aiaa.org | DOI: 10.2514/6.2019-4467

4.6 Boundary Conditions

The 3rd order accuracy no slip condition is enforced on the solid surface with the wall treatment suggested in [26] to achieve the flux conservation on the wall. The computational mesh is shown in Fig. 9. Total pressure, total temperature and flow angles are specified at the injection duct inlet, as well as the upstream portion of the far field. For the static condition, the static pressure at the downstream farfield is set to be equal to the total pressure at upstream far field. Constant static pressure is applied at the suction duct outlet as well as the downstream portion of the far field. The total mesh size is 91,440 for all 2D cases, split into 23 blocks for the parallel computation. The total mesh size is 23.168 million for 3D cases, split into 322 blocks for the parallel computation. The domain size is about 500 chords away from the airfoil to ensure a solid convergence at the static flow conditions. The airfoil is one chord above ground to mimic the VTOL ground effect. The first grid point on the wing surface is placed at $y^+ \approx 1$. The actuator disk BC is modeled as a flat surface, across which the static pressure is increased by a percentage ΔP based on the local static pressure upstream of the disk. Even though the pressure increase percentage is uniform across the dick, the pressure increase is not due to the non-uniform local static pressure upstream of the disk. The pressure jump across the disk is handled by the approximate Riemann solver in the FASIP code similar to a shock wave.

5 Results and Discussion

In this section, the results of CFJ-VTOL and CFJ-ESTOL are presented, including two VTOL 2D cases, two ESTOL 2D cases, and three VTOL 3D case. For the VTOL and ESTOL cases, two different actuator β angles are used ($\beta = 136°$ and $95°$). Other parameters are optimized for the a fixed β angle to obtain a system C_L about 20 (the first 6 cases) or 50 (the last case) with the least power consumption. The corresponding case parameters are listed in Table 1. All airfoils used in the current study are CFJ-NACA-6421. For the static condition, the freestream conditions have zero velocity and can not be used as reference condition to normalize the aerodynamic forces. Thus artificial freestream parameters at Mach of 0.04 are used to normalize the aerodynamic forces. These parameters include $V_\infty = 13.9m/s$, $\rho_\infty = 1.23$, which are used to calculate the reference dynamic pressure q.

In Table 1, the Mach number 0.0 is for the VTOL cases showing static condition. The Mach number of 0.04

is for the ESTOL cases showing the freestream Mach number at takeoff and landing. The C_μ is the CFJ airfoil injection momentum coefficient. ΔP is the strength of the propeller actuator disk showing the pressure rise across the actuator disk. For example, $\Delta P = 0.02$ means that the static pressure rise 2% across the actuator disk. AR is the aspect ratio.

Table 1: Simulation parameters used in the current work.

Cases	$Mach$	α	β	C_μ	ΔP	AR
C1	0.0	77.5°	136°	1.2	0.02	N/A
C2	0.0	74.5°	95°	0.6	0.02	N/A
C3	0.04	72°	136°	2.0	0.014	N/A
C4	0.04	65°	95°	0.8	0.014	N/A
C5	0.0	77.5°	136°	2.0	0.02	20
C6	0.0	75.5°	95°	2.0	0.02	10
C7	0.0	75.5°	95°	2.0	0.05	20

Downloaded by Gecheng Zha on September 27, 2019 | http://arc.aiaa.org | DOI: 10.2514/6.2019-4467

5.1 VTOL Performance

In this section, vertical takeoff/landing performance of the propeller-CFJ airfoils are investigated. Two cases (C1 and C2) with actuator angles β of 136° and 95°, and the associated α of 77.5° and 80° are studied. These two cases have about the same total system lift coefficient, but have different lift contribution between the propeller and the CFJ airfoil. The case with β of 136° exert a much higher flow turning on the CFJ airfoil than the case of β of 95°. The propeller of the former is more forward facing than the latter case. The higher flow turning on the let the CFJ airfoil generates more lift. Fig. 10 shows the Mach contours of these two cases with streamlines. The column on the left (a) and (c) are the results of case C1. The column on the right (b) and (d) are the results of case C2. Both the flows are very well attached attributed to the unique performance of the CFJ airfoil. The wakes hit the ground and and bifurcate to two sides. For case C1, the flow turns more around the CFJ airfoil due to the higher β angle, which leads to a much higher Mach number on the airfoil suction surface than the case C2.

As shown in Fig. 10 (a) and (b), the actuators withdraw the flow from all directions. The flow on the pressure surface of the airfoil is almost horizontal and creates an angle of attack about the same as α, which is 77.5° and 80° respectively. On the upper part of the CFJ airfoil, the flow is more perpendicular to the propeller disk and the angle of attack to the airfoil is not as high as on the pressure surface side. It is noted that there is a recirculating flow region at the tip of the propeller. However, such a recirculating flow is expected to exist for all propeller flows at static conditions. The stagnation points locate at the airfoil pressure surfaces for both cases, but more towards the airfoil trailing edge for case C1. For the far fields, which are presented in Fig. 10 (c) and (d), the flow structures are similar. Two large vortices can be observed in the upstream and downstream of the airfoil, respectively. The vortices are formed by the actuator disk suction effect and the ground blockage effect. The upstream vortex is larger than that of the downstream vortex, and the case C1 shows more asymmetry of the vortices due to greater actuator β angle.

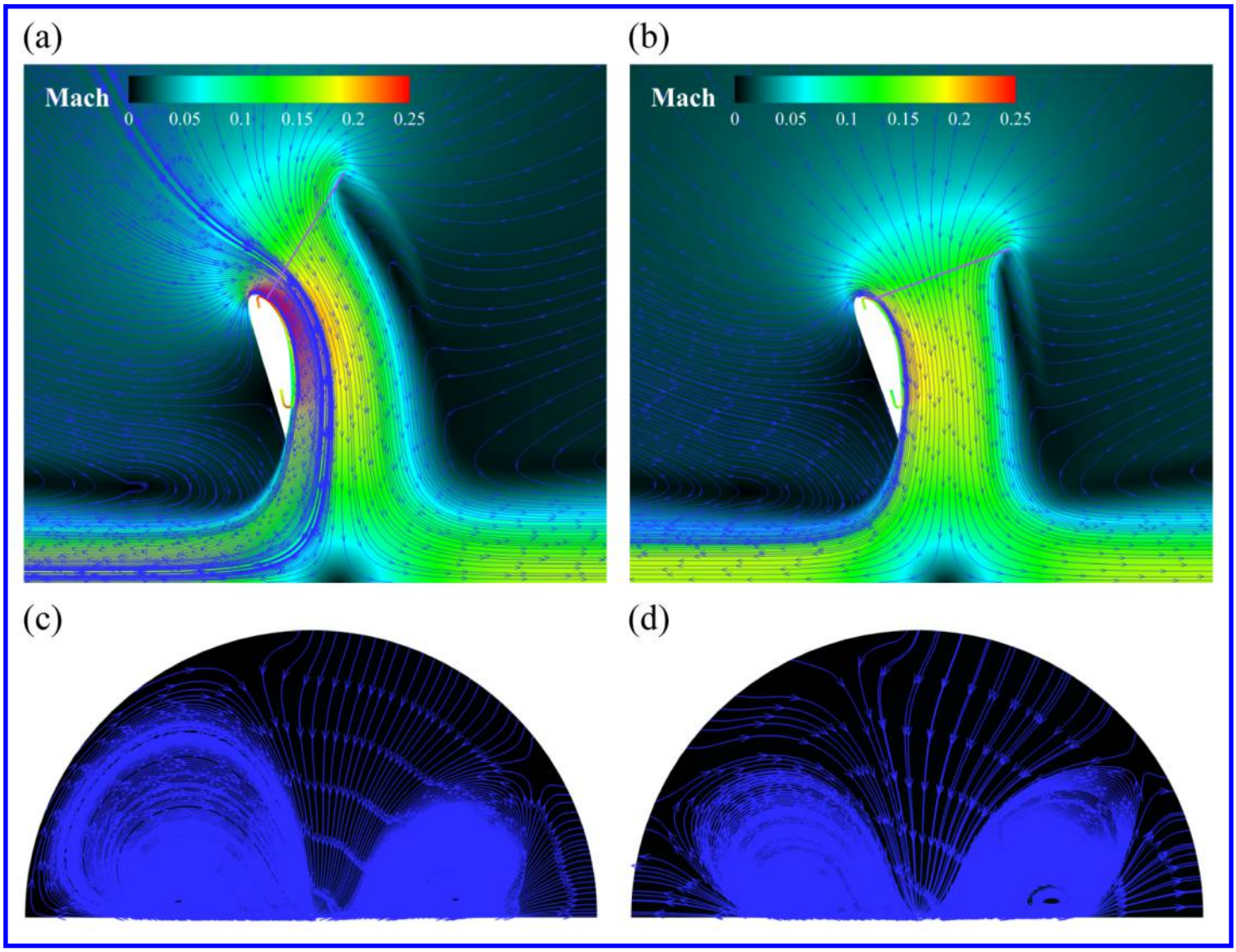

Figure 10: Streamlines in near and far flow field, (a) case C1 near field; (b) case C2 near field; (c) case C1 far field; (d) case C2 far field.

The pressure distributions on the airfoil surfaces are shown in Fig. 11. The discontinuities on the curves are due to the existence of the injection and suction slots of the CFJ. From the plot we can see that the C_P on the airfoil pressure surface is nearly zero for both cases since it is at the static condition for the VTOL cases. The $-C_P$ on the suction peak reaches over 70 for the case C1 due to a large flow turning induced by the actuator disk. The injection slots for both cases are downstream of the suction peak to benefit the low pumping power required, which is the key factor to generate a large lift from the CFJ airfoil at much lower power consumption than the propeller actuator disk.

Downloaded by Gecheng Zha on September 27, 2019 | http://arc.aiaa.org | DOI: 10.2514/6.2019-4467

Downloaded by Gecheng Zha on September 27, 2019 | http://arc.aiaa.org | DOI: 10.2514/6.2019-4467

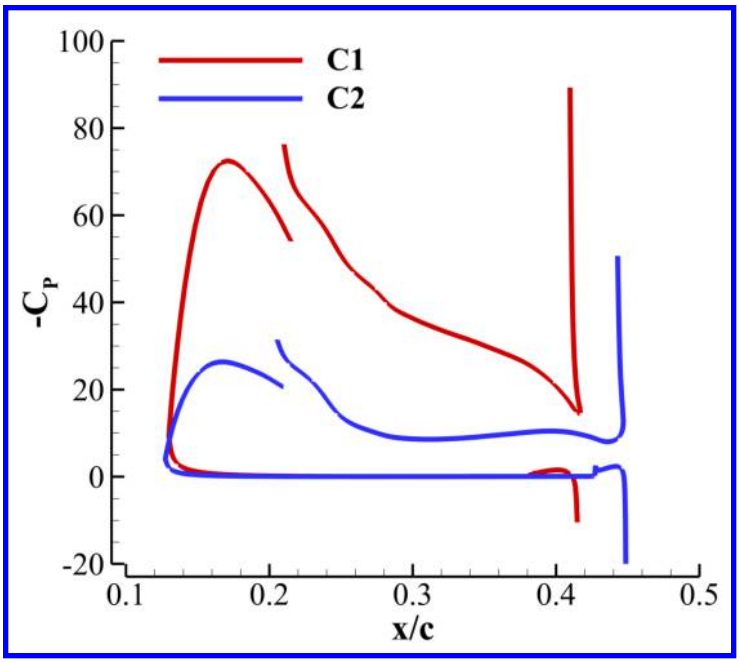

Figure 11: C_P distributions on the airfoil surface of case C1 and C2.

Table 2: Aerodynamic performance of case C1 and C2.

Cases	Items	C_μ	C_L	C_D	C_m	F_c	P_c	PR	M_j	DL_c	PL_c	ΔPL
C1	CFJ	1.2	12.62	15.09	-1.93	19.67	1.57	1.022	0.305	17.38	0.124	-24.57%
	Actuator		8.93	-14.91	-10.65	17.38	36.24				4.06	
	Total		21.55	0.18	-12.58	21.55	37.81				1.75	
C1*	N/A	N/A	21.55	0	N/A	21.55	50.02	N/A	N/A	21.55	2.32	
C2	CFJ	0.6	4.34	6.35	-1.35	7.69	0.47	1.009	0.216	17.79	0.108	-20.96%
	Actuator		16.67	-6.22	-5.05	17.79	37.54				2.25	
	Total		21.01	0.13	-6.40	21.01	38.00				1.81	
C2*	N/A	N/A	21.01	0	N/A	21.01	48.16	N/A	N/A	21.01	2.29	

Table 2 lists the aerodynamic performance of the two cases. Also listed are the corresponding theoretical evaluation of the power coefficient using the actuator disk only (C1* and C2*) for comparison. Case C1* and C2* produce the same amount of lift as the case C1 and C2, but all by ideal actuator disks facing completely upward as conventional VTOL.

For the force production, the case C1 shows a much greater airfoil resultant force coefficient of 19.67 than the case C2 of 7.69 due to a larger flow turning. The greater β of C1 results in a smaller lift produced by the actuator and a larger lift from the CFJ airfoil than C2. Table 2 also shows that the power loading of the CFJ airfoil is much less than the actuator disk, meaning that the CFJ airfoil contributes substantial lift at much lower power. For Case C1, the CFJ airfoil contributes 58.6% of the total lift, but only consumes 4.15% of the total power. For Case C2, the lift of CFJ is 20.7% of the total lift and the power is only 1.2% of the total power. Compared with the Case C2, case C1 has a greater CFJ P_c due to the CFJ generating higher lift requiring a high C_μ, but the Case C2 has about 20% lower CFJ airfoil power loading with a higher efficiency due to a lower lift coefficient. Larger C_μ is required for larger β angle to prevent the flow separation downstream of the actuator. The P_c of the actuator

are almost the same since the corresponding ΔP is the same for both cases. Compared with the corresponding actuator only, both case C1 and C2 show more than 20% power reduction in terms of the system power loading.

Due to the lift contribution from the CFJ airfoil, the disk loading of the propellers has a 20% reduction, which will greatly decrease the noise produced by the actuator. Since the propeller is on the top of the airfoil, the noise radiation downward will be substantially shielded by the airfoil. It will further reduce the overall system community noise. The maximum injection Mach number as indicated in Table 3 is about 0.3, which is desirable not to generate high speed jet noise.

5.2 ESTOL Performance

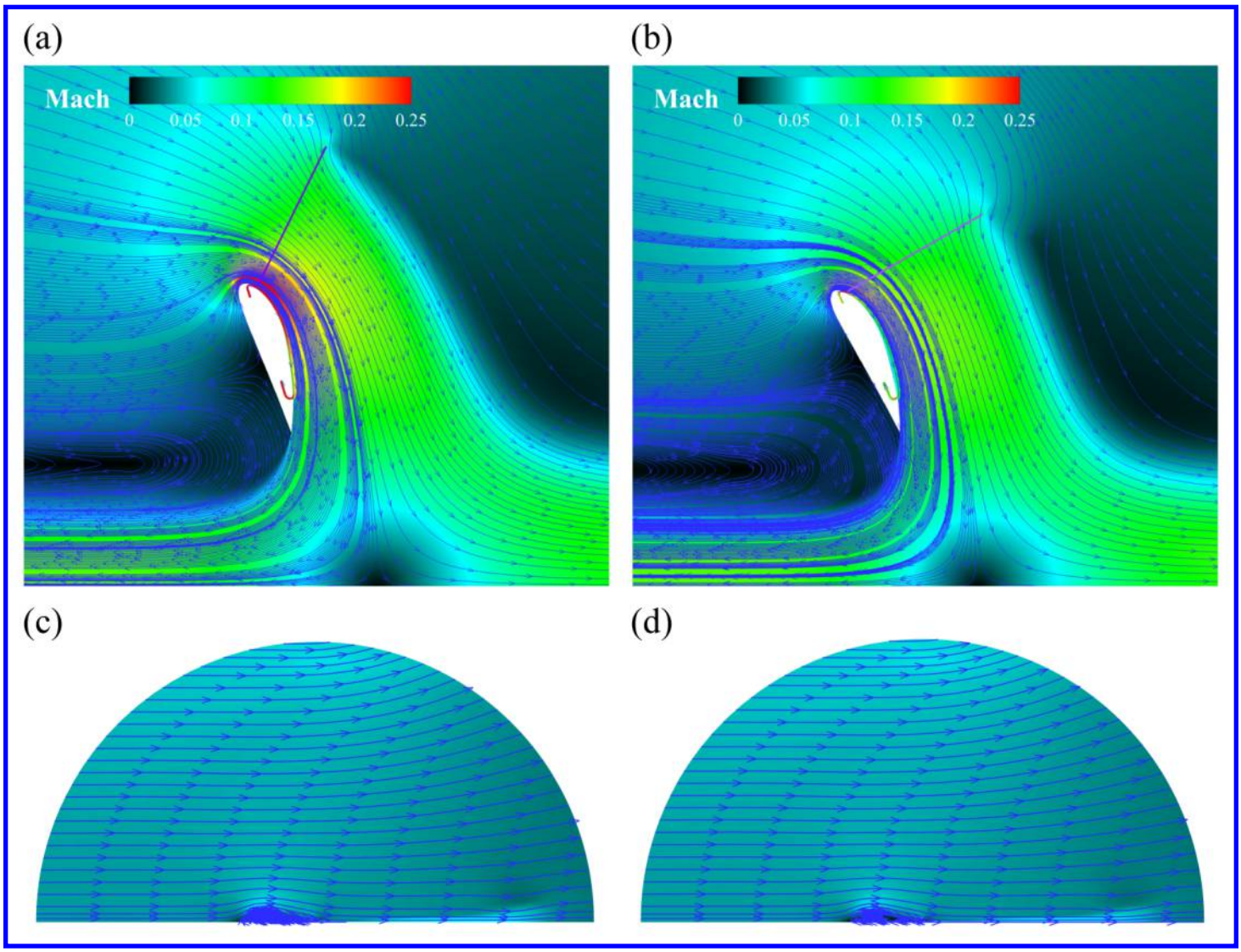

Figure 12: Streamlines in near and far flow field, (a) case C3 near field; (b) case C4 near field; (c) case C3 far field; (d) case C4 far field.

Downloaded by Gecheng Zha on September 27, 2019 | http://arc.aiaa.org | DOI: 10.2514/6.2019-4467

In this section, extreme short takeoff/landing performance of the propeller-CFJ airfoil systems are investigated. Only the takeoff condition that requires a thrust for acceleration is considered. The landing case with some system drag will be studied in future. As shown in Table 1, two cases (C3 and C4) with actuator angles β of 136° and 95°, and the associated α of 72° and 65° are studied. Note that the α of Case C3 and C4 are smaller than the VTOL case of C1 and C2 as shown in Table 1 because the system is rotated counter clockwise to generate some thrust for takeoff acceleration. As shown in Table 1, the incoming flow Mach number is 0.04, corresponding to 13.9m/s (31miles/h) at a seal level ambient temperature of 300°K. Fig. 12 shows the Mach contours of these two cases. Similar to the VTOL cases, the flow sustain a large turning and stay attached due to the CFJ capability. For the case C3, the flow turns more around the CFJ airfoil due to the higher β angle, which lead to a much higher Mach number on the airfoil suction surface.

For the far fields, which are presented in Fig. 12 (c) and (d), the flow structures are about the same since the incoming flow velocity is the same for both cases. However, they are very different from the VTOL cases at static condition, which generates two large vortices. AT the ESTOL condition, the flow at exit is tilted up due to ground effect. The downward jet hits the ground the is defected upward behind the airfoil. It make the overall outgoing flow slightly flow tilted up.

Downloaded by Gecheng Zha on September 27, 2019 | http://arc.aiaa.org | DOI: 10.2514/6.2019-4467

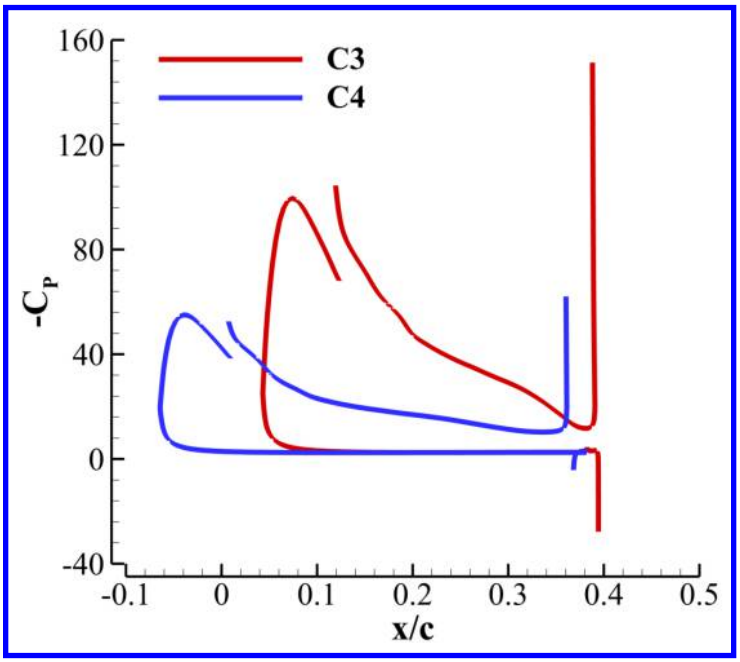

Figure 13: C_P distributions on the airfoil surface of case C3 and C4.

The pressure coefficient distributions on the CFJ airfoil surfaces are shown in Fig. 13. From the plot we can see that the $-C_P$ value of the Case C3 at the suction reaches over 100 due to the larger flow turning, substantially greater than that of the Case C4 of 60. Benefited from the freestream incoming flow, the $-C_P$ values on the suction surface are greater than those of the VTOL case, indicating greater lift coefficients.

Table 3 lists the aerodynamic performance of the above two cases. Also listed are the CFJ-VTOL cases with the same β angle for comparison. Similar to the VTOL cases, case C3 shows a much greater lift of the CFJ airfoil due to larger flow turning. Comparing C3 with C1, the CFJ power coefficient of C3 is larger because the flow turning is larger. However, the actuator power coefficient and the total power of C3 are substantially reduced. Note that the C_μ for ESTOL cases are greater than those of the VTOL cases as shown in Table 1. It is because of

Table 3: Aerodynamic performance of case C3 and C4.

Cases	Items	C_μ	C_L	C_D	C_m	F_c	P_c	PR	M_j	DL_c	PL_c	ΔPL
C3	CFJ	2.0	16.19	10.59	-1.20	19.35	3.59	1.039	0.405	12.23	0.222	-33.71%
	Actuator		5.3	-11.02	-8.00	12.23	21.39				4.04	
	Total		21.49	-0.43	-9.20	21.49	24.98				1.16	
C1	CFJ	1.2	12.62	15.09	-1.93	19.67	1.57	1.022	0.305	17.38	0.124	
	Actuator		8.93	-14.91	-10.65	17.38	36.24				4.06	
	Total		21.55	0.18	-12.58	21.55	37.81				1.75	
C4	CFJ	0.8	9.38	5.6	-1.02	10.92	0.82	1.014	0.252	12.22	0.087	-38.67%
	Actuator		10.54	-6.18	-5.49	12.22	21.36				2.03	
	Total		19.93	-0.58	-6.51	19.94	22.18				1.11	
C2	CFJ	0.6	4.34	6.35	-1.35	7.69	0.47	1.009	0.216	17.79	0.108	
	Actuator		16.67	-6.22	-5.05	17.79	37.54				2.25	
	Total		21.01	0.13	-6.40	21.01	38.00				1.81	

Downloaded by Gecheng Zha on September 27, 2019 | http://arc.aiaa.org | DOI: 10.2514/6.2019-4467

the CFJ need more energy to control the flow when there is incoming flow. Consequently, the P_c of the CFJ for the ESTOL cases are also greater than those of the VTOL cases. Moreover,the P_c of the actuator are significantly reduced compared with the VTOL case. Compared with the corresponding CFJ-VTOL cases, the case C3 and C4 show about 35% power saving in terms of power loading. Also, they show about 30% reduction of the disk loading. The maximum injection Mach number is increased to 0.4 from 0.3 due to the stronger CFJ, but still at fairly low level for jet noise. In general, the ESTOL of the CFJ airfoil substantially reduce the power consumption compared with its VTOL counterparts with lower noise due to reduced lower disk loading.

5.3 VTOL Performance of 3D CFJ Wings

The vertical takeoff/landing performance of 3D CFJ-VTOL system (C5, C6, and C7) is evaluated. The case configurations are listed in Table 1. Case C5 is a 3D straight wing stacked along the span using the 2D configuration of C1 with an aspect ratio of 20 and no sweep and taper. The Case C6 is modified from C5 with the actuator angle β reduced to 95° from 135° and the AR is reduced to 10, also the α angle is decreased from 77.5° to 75.5°. For case C7, the actuator strength ΔP is increased from 0.02 to 0.05 and the AR is set to 20 with all other conditions the same as Case C6. A Symmetric boundary condition is applied at the wing root and a zero gradient boundary condition is used in the span wise far field boundary. Wing tip is modeled and no slip wall boundary condition is applied to study the tip effect. The results for case C5, including the flow field, wing surface pressure, and aerodynamic performance are presented in detail. For the other two cases (C6 and C7), the aerodynamic performance are tabulated for comparison.

Fig. 14 shows the Mach contour slices along the wing span of case C5. Similar to the 2D VTOL cases, most of the inner slices show that flow stay attached to the airfoil suction surface. However, due the wing tip effect, the flow is detached from the wing in the wing tip region. As a result, the Mach number near the suction surface of the wing tip region decreases, and the wake near the wing tip propagats more toward downstream.

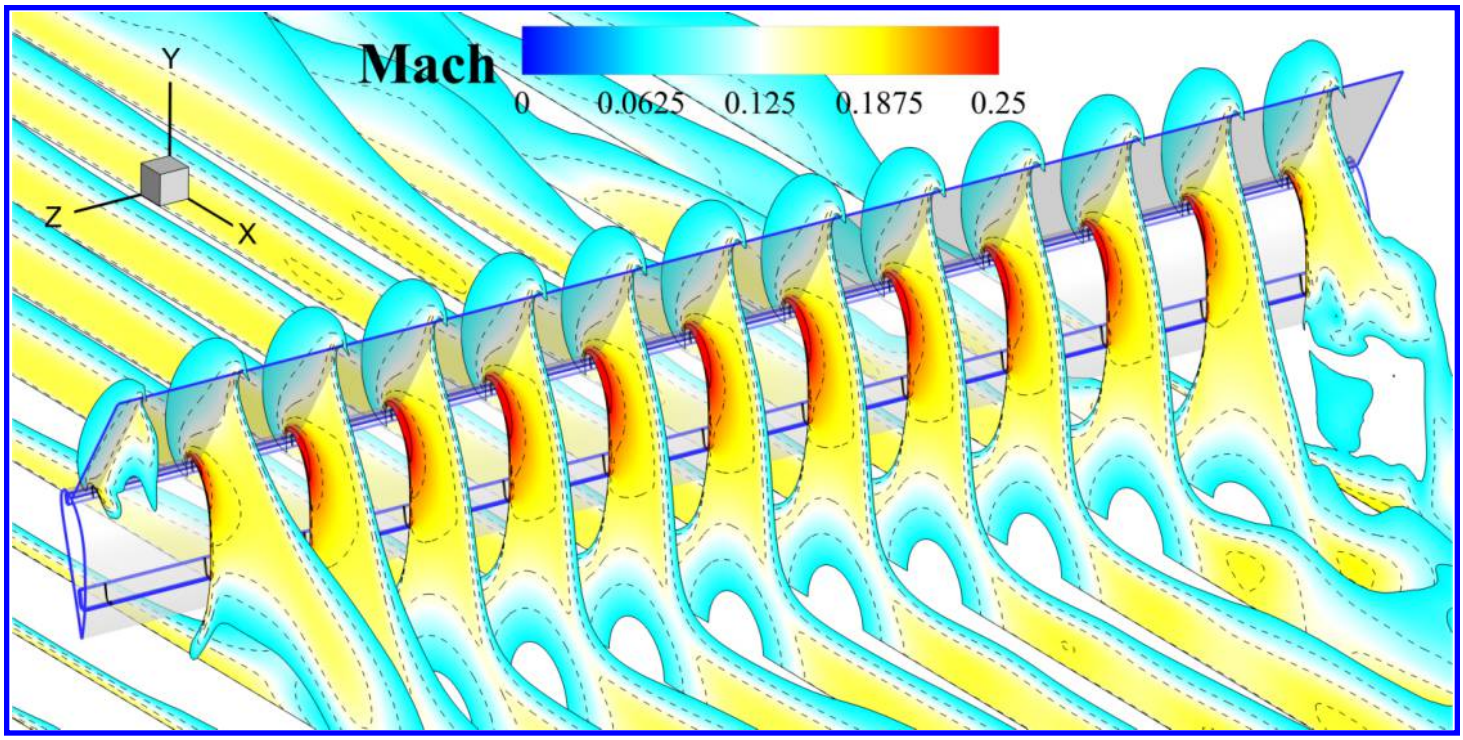

Figure 14: Mach contour slices along the wing span for case C5.

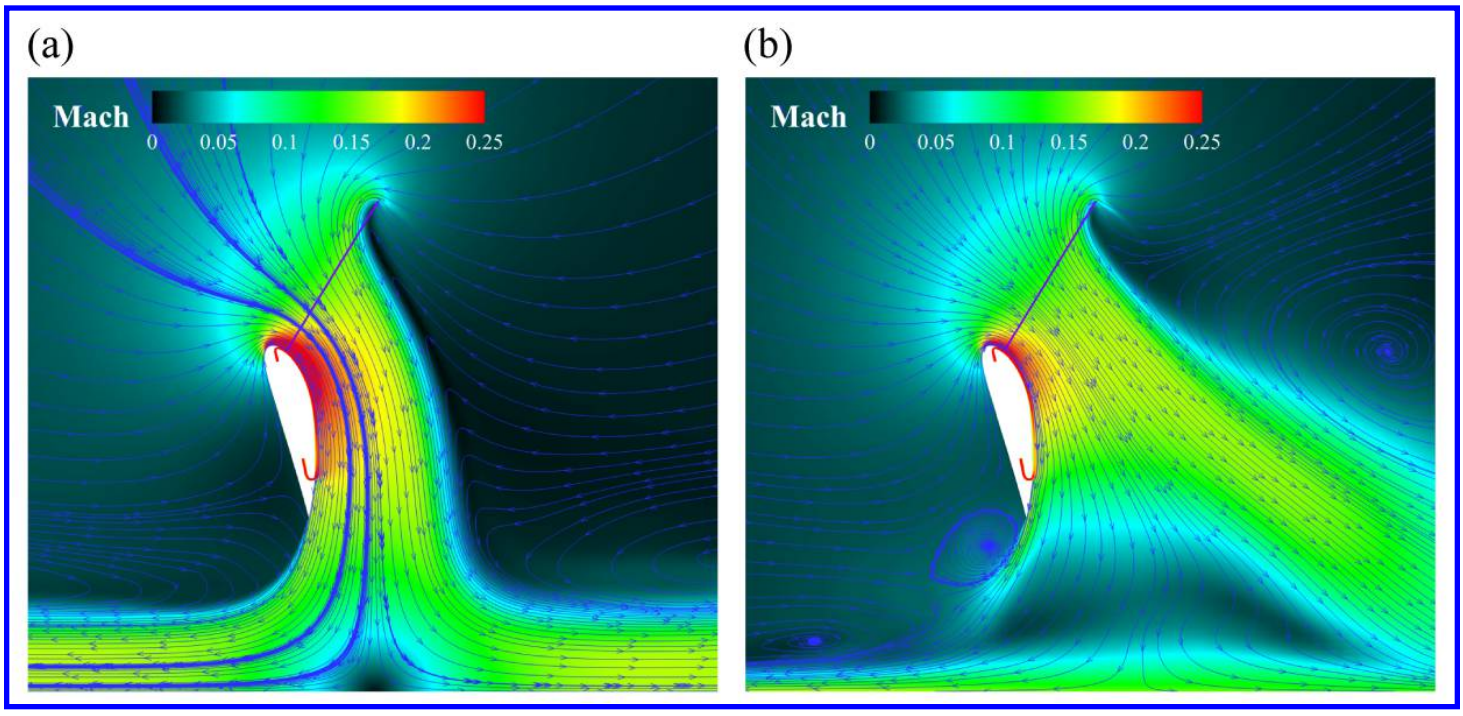

Figure 15: Streamlines around the wing section at (a) mid wing slice section and (b) wing tip region slice.

Fig. 15 shows the streamlines around the wing section at two different wing span locations, mid span (Fig. 15 a) and wing tip at 98% span (Fig. 15 b). It can be seen that the streamlines and flow structures at the mid span

Downloaded by Gecheng Zha on September 27, 2019 | http://arc.aiaa.org | DOI: 10.2514/6.2019-4467

slice are almost the same as those of the case C1 (Fig. 10 a). However, for the wing section at the wing tip, the flow structures become more complicated. The tip vortex is shown on the pressure side of the flow field. Two smaller vortices are also induced on the suction side of the flow. The overall wake flows more downstream instead of toward ground as in the mid-sections.

Fig. 16 shows the pressure contour on the wing surface. The surface pressure distribution along the wing span is fairly uniform except in the wing tip region. For the wing suction surface, the pressure increases near the wing tip due to the flow separation. For the wing pressure surface, the C_P value is near zero since the flow on the pressure side does not have much velocity and dynamic pressure from the static condition, which provides the high pressure generating the high lift.

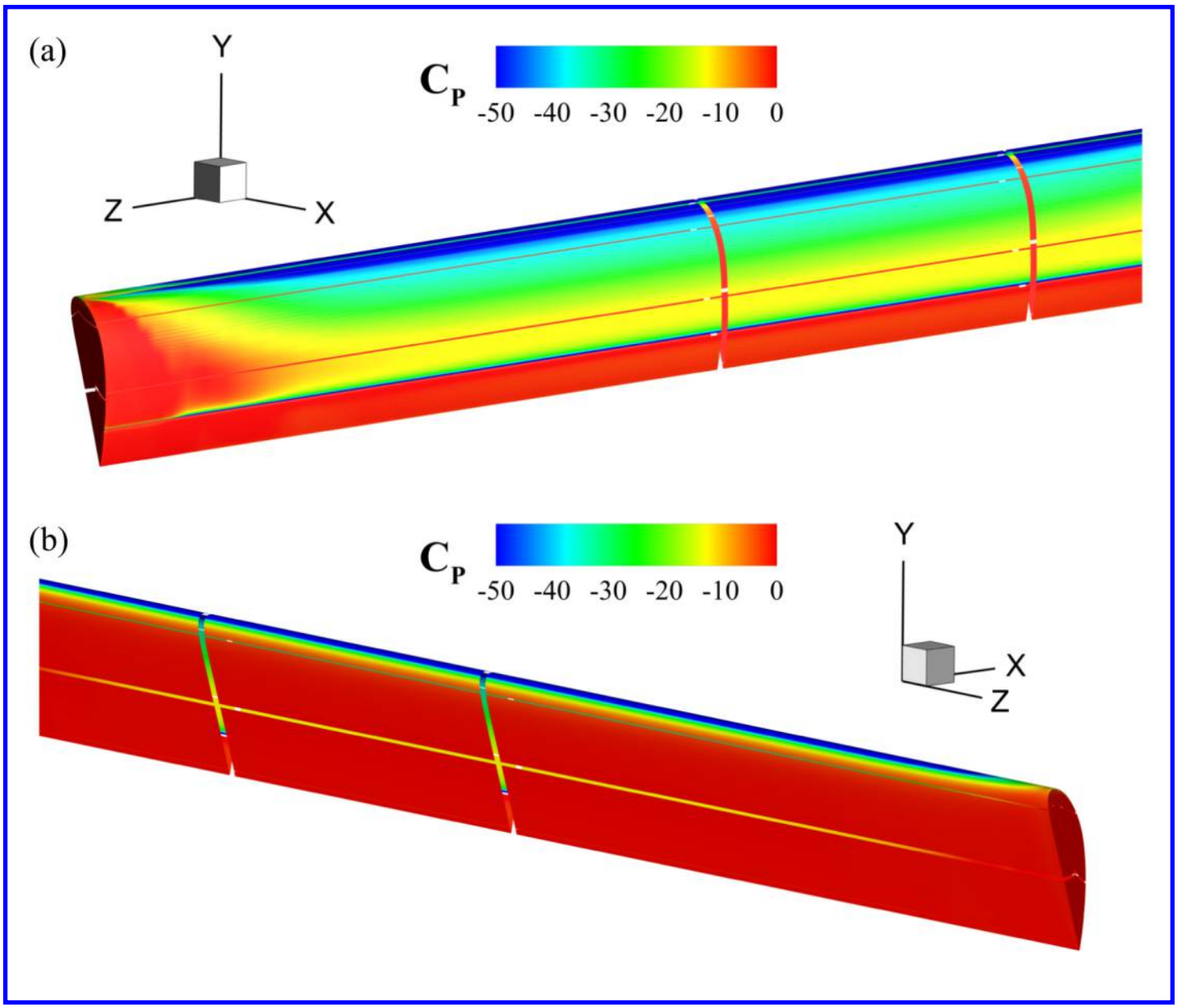

Figure 16: Surface pressure distribution on the wing for case C5. (a) Suction surface pressure distribution; (b) pressure surface pressure distribution.

Downloaded by Gecheng Zha on September 27, 2019 | http://arc.aiaa.org | DOI: 10.2514/6.2019-4467

Table 4: Aerodynamic performance of case C5, C6, and C7.

Cases	Items	AR	C_μ	C_L	C_D	C_m	F_c	P_c	PR	M_j	DL_c	PL_c	ΔPL
C5	CFJ	20	2.0	12.05	11.65	-1.30	16.76	4.44	1.048	0.410	17.23	0.368	-15.72%
	Actuator			8.87	-14.81	-10.60	17.23	35.86				4.04	
	Total			20.92	-3.16	-11.90	21.16	40.31				1.93	
C5*	N/A	N/A	N/A	20.92	0	N/A	20.92	47.84	N/A	N/A	20.92	2.29	
C6	CFJ	10	2.0	4.74	5.65	-1.24	7.34	4.95	1.053	0.392	17.78	1.04	-14.47%
	Actuator			16.04	-6.16	-5.26	17.78	35.62				2.22	
	Total			20.78	-0.50	-6.50	20.79	40.56				1.95	
C6*	N/A	N/A	N/A	20.78	0	N/A	20.78	47.36	N/A	N/A	20.78	2.28	
C7	CFJ	20	2.0	11.21	15.11	-3.19	18.81	3.20	1.035	0.403	42.83	0.285	-21.79%
	Actuator			39.99	-15.34	-13.13	42.83	140.15				3.50	
	Total			51.20	-0.23	-16.32	51.20	143.35				2.80	
C7*	N/A	N/A	N/A	51.20	0	N/A	51.20	183.16	N/A	N/A	51.20	3.58	

Downloaded by Gecheng Zha on September 27, 2019 | http://arc.aiaa.org | DOI: 10.2514/6.2019-4467

Table 4 lists the aerodynamic performance of all the 3D cases (C5, C6, and C7) and the corresponding cases with the lift generated by the propeller actuator only case (C5*, C6*, and C6*) for comparison.

For case C5, comparing to the 2D VTOL case C1, the C_μ is increased from 1.2 to 2.0 to maintain the flow attachment. the lift of the wing is similar whereas the drag of the wing is decreased due to the increased C_μ. The actuator forces for the 2D and 3D cases are the same due to the same actuator ΔP. All these factors lead to the overall 3D CFJ-VTOL wing have about the same amount of lift as the case C1 and a little higher thrust. For the power consumption, the CFJ P_c of the 3D Case 5 is much higher than the 2D Case C1. It is because a higher C_μ is needed for the 3D case to overcome the wing tip effect. The power loading for the case C5 is 9.8% higher than the case C1, while the disk loading remains the same. Comparing to the corresponding case using actuator only (C5*), the power loading is reduced by 15.72% and the disk loading is reduced by 17.64%.

For case C6, the wing aspect ratio is reduced to 10 and the actuator angle β is reduced to 95°. Due to a smaller flow turning and greater a 3D effect (lower aspect ratio), the resultant force generated by the CFJ-VTOL wing is decreased compared with the Case C5. However, the power loading is reduced by 14.47% comparing to the case using the propeller actuator only(C5*).

For case C7, the actuator strength ΔP is increased to 0.05 to see the effect. The β angle is 95° and the wing aspect ratio is 20. Both disk loading and power loading are greatly increased to generate more total system lift. Comparing to the case with lift generated by the propeller actuator only case C7*, the power loading reduction is 21.79%. This indicates that the efficiency of CFJ-VTOL is even more enhanced at higher disk loading and higher system lift coefficient.

The maximum injection Mach number at 3D is increased to 0.4 from 0.3 of 2D due to the stronger CFJ, but still at fairly low level for jet noise.

Fig. 17 shows the VTOL performance comparison with the theoretical limit in terms of power loading versus disk loading adopted from [1]. Most of the current VTOL aircraft can be found in the plot. The green curve shows the theoretical limit of 2D actuator disks at hovering condition. At a same disk loading, all of the five CFJ-VTOL cases have lower power loadings than the theoretical limit. It is not because the disk is more efficient, but because the wing contributes to the lift of the overall system. When the system is moved form 2D to 3D, the power loading of a CFJ-wing with an aspect ratio of 20 suffers little loss of the power loading advantage when the 3D disk loading is high at a disk loading coefficient of 43. When the 3D disk loading coefficient is below 20, the

power loading is increased about 5%.

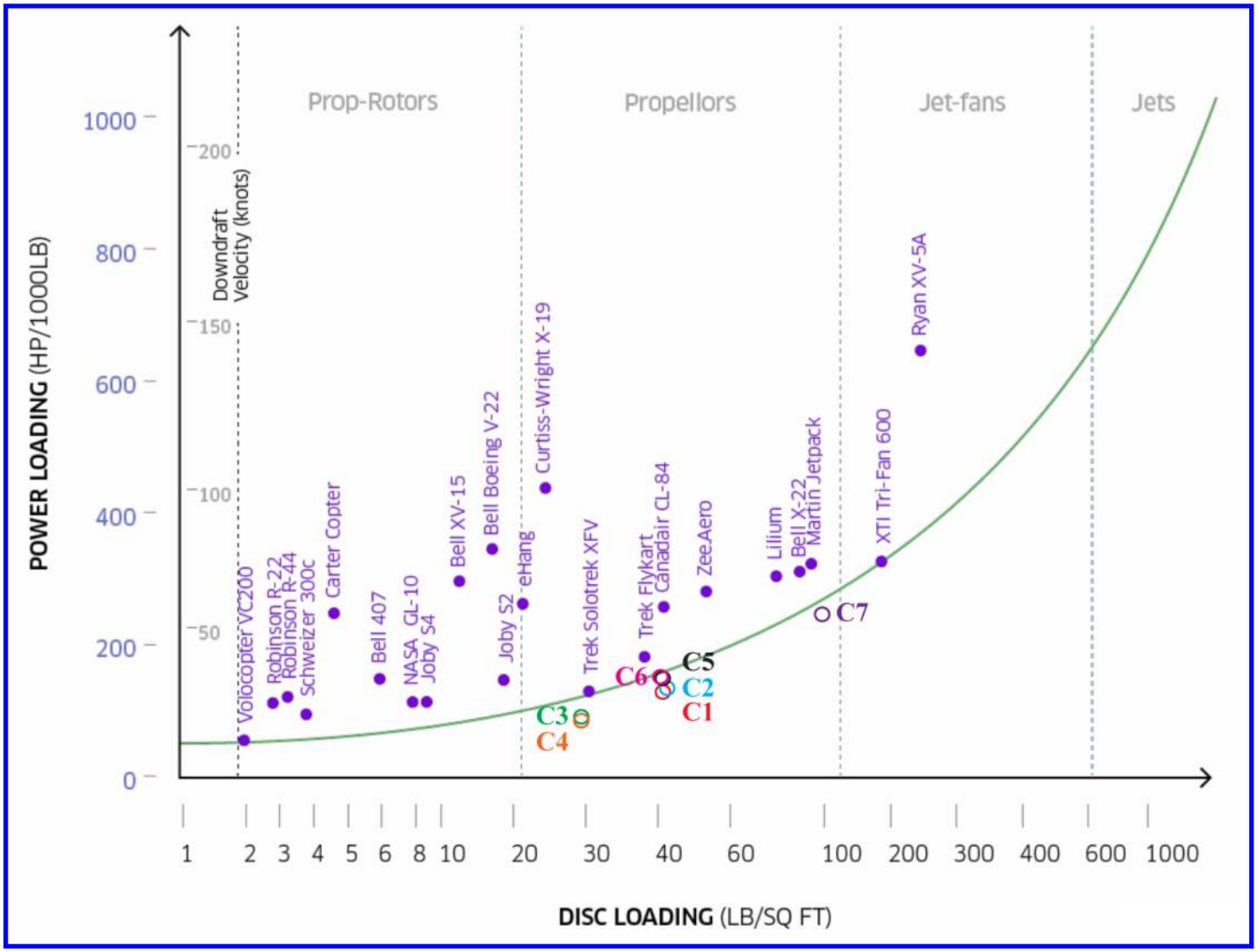

Figure 17: VTOL flight performance map in terms of power loading versus disk loading.

6 Conclusions

The integrated CFJ-VTOL system with the propellers mounted above a CFJ wing is studied conceptually by numerical simulation at static conditions. The same system can be potentially used either for VTOL or ESTOL depending on the situation with significantly reduced takeoff power and noise. Different from the conventional VTOL systems that rely solely on the propellers completely facing upward to generate the vertical lift, the propellers of the CFJ-VTOL system face forward and upward and only generate a part of the total lift. An important function of the propellers is to pull flow to the CFJ airfoil at static condition. The CFJ airfoil then generates very high lift coefficient at extraordinarily high angle of attack (e.g. $> 77°$) with a much lower power consumption rate than the propellers. For Case C1 with $\beta = 135°$, the CFJ airfoil contributes 58.6% of the total lift, but only consumes 4.15% of the total power. For Case C2 with $\beta = 95°$, the lift of CFJ is 20.7% of the total lift and the

Downloaded by Gecheng Zha on September 27, 2019 | http://arc.aiaa.org | DOI: 10.2514/6.2019-4467

power is only 1.2% of the total power. In other words, the CFJ-VTOL makes use of the CFJ wing to generate substantial or even the majority of the lift at vertical takeoff and landing, whereas the wings of conventional VTOL aircraft generate no lift at takeoff and landing even though they produce all the lift at cruise. Such an integrated CFJ-VTOL system has the potential to reduce the power loading by 20% or more at the VTOL phase. For the same lift coefficient, the disk loading is reduced by about 20% with a benefit to potentially decrease the noise. Furthermore, the upper wing mounted propeller is shield by the wing to mitigate downward radiating noise of the propeller. The CFJ-VTOL system hence is also potentially much quieter than the conventional VTOL. The maximum injection jet Mach number is 0.3 - 0.4, is at fairly low level for jet noise. When the system is moved form 2D to 3D, the power loading of a CFJ-wing with an aspect ratio of 20 suffers little loss of the power loading advantage when the 3D disk loading is high at a disk loading coefficient of 43. When the 3D disk loading coefficient is below 20, the power loading is increased about 5%. The resultant force of the the propeller-CFJ airfoil system at the static condition is controlled by the airfoil orientation angle (treated as AoA). By rotating the same propeller-CFJ airfoil system nose down, the system can generate both very high lift and thrust for ESTOL. For a takeoff speed of 13.9 m/s (Mach 0.04), the CFJ-ESTOL system further reduces the disk loading by 30% and the power loading by 35% compared with the CFJ-VTOL system. The ESTOL system is thus expected to be much more quiet and energy efficient.

Downloaded by Gecheng Zha on September 27, 2019 | http://arc.aiaa.org | DOI: 10.2514/6.2019-4467

7 Acknowledgment

We greatly appreciate the support by NASA Langley Center via National Institute of Aerospace monitored by Paul M. Rothhaar, and Mark More before he left NASA. We also thank Michal Patterson at NASA Langley center for his support and many very helpful discussions. We are also very grateful to Emil Buehler Perpetual Trust for their support for our research on green aviation at the University of Miami.

References

[1] Uber Elevate, "Fast-Forwarding to a Future of On-Demand Urban Air Transportation." Uber White Paper, Oct. 27, 2016.

[2] G.-C. Zha, W. Gao, and C. Paxton, "Jet Effects on Co-Flow Jet Airfoil Performance," *AIAA Journal, No. 6,*, vol. 45, pp. 1222–1231, 2007.

[3] G.-C. Zha and D. C. Paxton, "A Novel Flow Control Method for Airfoil Performance Enhancement Using Co-Flow Jet." *Applications of Circulation Control Technologies*, Chapter 10, p. 293-314, Vol. 214, Progress in Astronautics and Aeronautics, AIAA Book Series, Editors: Joslin, R. D. and Jones, G.S., 2006.

[4] G.-C. Zha, C. Paxton, A. Conley, A. Wells, and B. Carroll, "Effect of Injection Slot Size on High Performance Co-Flow Jet Airfoil," *AIAA Journal of Aircraft*, vol. 43, 2006.

[5] G.-C. Zha, B. Carroll, C. Paxton, A. Conley, and A. Wells, "High Performance Airfoil with Co-Flow Jet Flow Control," *AIAA Journal*, vol. 45, 2007.

[6] Wang, B.-Y. and Haddoukessouni, B. and Levy, J. and Zha, G.-C., "Numerical Investigations of Injection Slot Size Effect on the Performance of Co-Flow Jet Airfoil ," *AIAA Journal of Aircraft*, vol. 45, pp. 2084–2091, 2008.

[7] B. P. E. Dano, D. Kirk, and G.-C. Zha, "Experimental Investigation of Jet Mixing Mechanism of Co- Flow Jet Airfoil." AIAA-2010-4421, 5th AIAA Flow Control Conference, Chicago, IL, 28 Jun - 1 Jul 2010.

[8] B. P. E. Dano, G.-C. Zha, and M. Castillo, "Experimental Study of Co-Flow Jet Airfoil Performance Enhancement Using Micro Discreet Jets." AIAA Paper 2011-0941, 49th AIAA Aerospace Sciences Meeting, Orlando, FL, 4-7 January 2011.

[9] Lefebvre, A. and Dano, B. and Bartow, W. and Di Franzo, M. and Zha, G.-C., "Performance Enhancement and Energy Expenditure of Co-Flow Jet Airfoil with Variation of Mach Number." AIAA Paper 2013-0490, AIAA Journal of Aircraft, DOI: 10.2514/1.C033113, 2016.

[10] Lefebvre, A. and Zha, G.-C., "Numerical Simulation of Pitching Airfoil Performance Enhancement Using Co-Flow Jet Flow Control." AIAA Paper 2013-2517, AIAA Applied Aerodynamics Conference, San Diego, CA, 24 - 27 June 2013.

[11] Lefebvre, A. and Zha, G.-C. , "Design of High Wing Loading Compact Electric Airplane Utilizing Co-Flow Jet Flow Control." AIAA Paper 2015-0772, AIAA SciTech2015: 53nd Aerospace Sciences Meeting, Kissimmee, FL, 5-9 Jan 2015.

[12] Lefebvre, A. and Zha, G.-C., "Trade Study of 3D Co-Flow Jet Wing for Cruise and Takeoff/Landing Performance." AIAA Paper 2016-0570, AIAA SCITECH2016, AIAA Aerospace Science Meeting, San Diego, CA, 4-8 January 2016.

[13] Liu, Z.-X. and Zha, G.-C., "Transonic Airfoil Performance Enhancement Using Co-Flow Jet Active Flow Control." AIAA Paper 2016-3472, AIAA AVIATION 2016, 8th AIAA Flow Control Conference, Washington, D.C, June 13-17, 2016.

[14] Yang, Y.-C. and Zha, G.-C., "Super-Lift Coefficient of Active Flow Control Airfoil: What Is the Limit?." AIAA Paper 2017-1693, AIAA SCITECH2017, 55th AIAA Aerospace Science Meeting, Grapevine, Texas, 9-13 January 2017.

[15] G.-C. Zha, Y.-C. Yang, Y. Ren, and B. McBreen, "Super-lift and thrusting airfoil of coflow jet-actuated by micro-compressors." AIAA Paper 2017-3061, AIAA AVIATION 2018, Atlanta, GA , 25 - 29 June 2018.

[16] A. Smith, "High-Lift Aerodynamics," *Journal of Aircraft*, vol. 12, pp. 501–530, 1975.

[17] G.-C. Zha, "Estol performance for heavy lift transports using ultra-high lift high efficiency co-flow jet airfoil." Final Report to DARPA for Contract HR0011-16-2-0052, May 25, 2018.

[18] Y.-Q. Shen and G.-C. Zha, "Large Eddy Simulation Using a New Set of Sixth Order Schemes for Compressible Viscous Terms ," *Journal of Computational Physics*, vol. 229, pp. 8296–8312, 2010.

[19] Zha, G.C., Shen, Y.Q. and Wang, B.Y., "An improved low diffusion E-CUSP upwind scheme ," *Journal of Computer and Fluids*, vol. 48, pp. 214–220, Sep. 2011.

[20] Y.-Q. Shen and G.-Z. Zha , "Generalized finite compact difference scheme for shock/complex flowfield interaction," *Journal of Computational Physics*, vol. doi:10.1016/j.jcp.2011.01.039, 2011.

[21] Shen, Y.-Q. and Zha, G.-C. and Wang, B.-Y., " Improvement of Stability and Accuracy of Implicit WENO Scheme," *AIAA Journal*, vol. 47, No. 2, pp. 331–344, 2009.

[22] Shen, Y.-Q. and Zha, G.-C. and Chen, X.-Y., " High Order Conservative Differencing for Viscous Terms and the Application to Vortex-Induced Vibration Flows," *Journal of Computational Physics*, vol. 228(2), pp. 8283–8300, 2009.

Downloaded by Gecheng Zha on September 27, 2019 | http://arc.aiaa.org | DOI: 10.2514/6.2019-4467

▶[23] Shen, Y.-Q. and Zha, G.-C. , " Improvement of the WENO Scheme Smoothness Estimator," *International Journal for Numerical Methods in Fluids*, vol. DOI:10.1002/fld.2186, 2009.

▶[24] G.-C. Zha and E. Bilgen, "Numerical Study of Three-Dimensional Transonic Flows Using Unfactored Upwind-Relaxation Sweeping Algorithm," *Journal of Computational Physics*, vol. 125, pp. 425–433, 1996.

▶[25] B.-Y. Wang and G.-C. Zha, "A General Sub-Domain Boundary Mapping Procedure For Structured Grid CFD Parallel Computation," *AIAA Journal of Aerospace Computing, Information, and Communication*, vol. 5, No.11, pp. 2084–2091, 2008.

▶[26] Y.-Q. Shen, G.-C. Zha, and B.-Y. Wang, "Improvement of Stability and Accuracy of Implicit WENO Scheme ," *AIAA Journal*, vol. 47, pp. 331–344, 2009.

Downloaded by Gecheng Zha on September 27, 2019 | http://arc.aiaa.org | DOI: 10.2514/6.2019-4467